Chemical Engineering Journal 454 (2023) 140118

Contents lists available at ScienceDirect

Chemical Engineering Journal

journal homepage: www.elsevier.com/locate/cej

3D-printed cardiovascular polymer scaffold reinforced by functional nanofiber additives for tunable mechanical strength and controlled drug release

Yun-Jin Jeong [a,b,1], Songah Jeong [c,1], Seokjae Kim [a,d,1], Hea Ji Kim [c], Juyeong Jo [d], Arunkumar Shanmugasundaram [a,b], Hyungwoo Kim [c,*], Eunpyo Choi [a,d,*], Dong-Weon Lee [a,b,e,*]

[a] School of Mechanical Engineering, Chonnam National University, 77 Yongbong-ro, Buk-gu, Gwangju 61186, Republic of Korea
[b] Advanced Medical Device Research Center for Cardiovascular Disease, Chonnam National University, 77 Yongbong-ro, Buk-gu, Gwangju 61186, Republic of Korea
[c] School of Polymer Science and Engineering, Chonnam National University, 77 Yongbong-ro, Buk-gu, Gwangju 61186, Republic of Korea
[d] Korea Institute of Medical Microrobotics, Cheomdangwagi-ro 208-beon-gil, Buk-gu, Gwangju 61011, Republic of Korea
[e] Center for Next-generation Sensor Research and Development, Chonnam National University, 77 Yongbong-ro, Buk-gu, Gwangju 61186, Republic of Korea

ARTICLE INFO

Keywords:
Macroscopic gold particles
Carbon nanofibers
Cardiovascular scaffolds
Cytocompatibility
X-ray imaging
Controlled drug release

ABSTRACT

Controlled drug eluting cardiovascular scaffolds (CDECS) have received significant interest in human healthcare compared to conventional drug eluting cardiovascular scaffolds (DECS) owing to their improved efficiency, patient compliance, and reduced toxicity. However, experimental demonstration of CDECS using synthetic polymers have had minimal success to yet. Herein, we proposed the use of gold particles incorporated carbon nanofibers (Au-S-CNF; hereafter referred to as functional additives) that are capable of reinforcing polycaprolactone (PCL) cardiovascular scaffolds and facilitating controlled drug delivery. The incorporation of 0.5 wt % of the designed functional additives uniformly dispersed in PCL matrix and cause superior mechanical properties (elastic modulus, 169 *MPa* and toughness, 334 $J\ cm^{-3}$) to that of bare PCL scaffolds. The functional additives reinforced PCL composites are used to fabricate patient specific CDECS using a 3-dimensonal (3D) printing technique. The practical feasibility of the proposed CDECS is established by demonstrating the scaffold's visibility in a mouse thoracic cavity using real-time X-ray imaging. Finally, the functional additives reinforced PCL cardiovascular scaffold used as a DECS and on-demand CDECS triggered by a near infrared (NIR) light source. This proposed medical device has the great potential to be employed for targeted therapies such as atherosclerosis, cancer, and tissue engineering.

1. Introduction

Cardiovascular diseases (CVDs) account for most deaths worldwide. According to the world health organization, each year 17.9 million people die from CVDs which account 32% of all global fatalities.[1–3] The primary pathophysiology of CVDs is atherosclerosis, generally caused by plaque formation on the artery wall, which gradually narrows arteries and restrict blood flow.[4–6] The most established therapy for atherosclerosis is stenting, in which permanent stents are implanted into constricted blood arteries to physically open the arteries to restore blood flow. Despite significant advancements, metal stents are often result in late complications, including thrombosis, endothelial dysfunction, stent strut uncovering, and in-stent restenosis which pose serious risks to patients.[7–9] Besides, the conventional metal stents may potentially interfere with computed tomography and magnetic resonance imaging. To mitigate these drawbacks, several alternatives have been explored including bioresorbable DECS. [10,11].

Several bioresorbable DECS, including magnesium (Mg), iron (Fe), and zinc (Zn), have been proposed for cardiovascular applications during the last two decades.[12,13] The proposed metal alloy stents exhibit excellent rates of biocompatibility, procedural success, and safety. However, the rapid corrosion rates of Mg-based DECS, the slow degradation rates of Fe-based DECS, and the poor mechanical strength of Zn-based DECS limit their usage.[12,13] The polymer based DECS such as

* Corresponding authors at: School of Mechanical Engineering, Chonnam National University, 77 Yongbong-ro, Buk-gu, Gwangju 61186, Republic of Korea.
E-mail addresses: kimhw@jnu.ac.kr (H. Kim), eunpyochoi@jnu.ac.kr (E. Choi), mems@jnu.ac.kr (D.-W. Lee).
[1] These authors contributed equally to this work.

https://doi.org/10.1016/j.cej.2022.140118
Received 18 August 2022; Received in revised form 10 October 2022; Accepted 27 October 2022
Available online 9 November 2022

based on poly(L-lactic acid) (PLLA), polyglycolide, poly(D,L-lactic-*co*-glycolic acid) (PLGA), polypropylene fumarate, polyanhydride, polycaprolactone (PCL), etc. have been intensively studied.[14,15] Among them, PLA and PCL have received considerable attention and approved by FDA for several biomedical applications. However, the practical feasibility of PLA is met with limited success owing to their brittle nature and low toughness.[16] The PCL-based cardiovascular scaffolds have superior flexibility and toughness, excellent biocompatibility, less acetic breakdown products, a low glass transition temperature, chemical compatibility with several drugs, slower degradation than other bioresorbable cardiovascular scaffolds, making them suitable for easy fabrication and prolonged drug administration.[17,18] To date, numerous PCL based scaffolds have been fabricated using the conventional electrospinning, free drying, laser micro cutting, and 3D printing techniques.[19–25] The nano/microscale fiber with interconnected porous architectures of the electrospun scaffolds are similar to the extracellular matrix present in natural tissues, and they show tremendous potential for accelerating the development of synthetic functional tissues.[26] Although electrospinning technology is simple to use, it is not optimal for producing complex vascular stent architectures and is mostly used for producing small-caliber stents or coating metal stents, resulting in limited application.[26] Another key technology that has greatly expanded the field of scaffold fabrication is free drying. However, the use of a mold in the fabrication of cardiovascular scaffolds may modify the scaffolds' structure when changing the concentration and viscosity of polymers and nanostructures, etc. Although, the laser microcutting delivers exceptional accuracy for surface structure, it is not appropriate for personalized DECS fabrication, and thermal effects may modify the polymer properties.[22,23] The additive manufacturing method possess excellent advantageous compared to other techniques such as short printing cycle, high material utilization, complex printable structure, and various sizes of vascular scaffolds. Besides, the additive manufacturing offers a cost-effective method for patient specific customized DECS which could potentially improve vessel patency.[24,25] Several research efforts have intensively studied the surface morphology and effect of geometric and fabrication factors on 3D printed PCL cardiovascular scaffolds' mechanical properties.[22,24,27] For instance, Park et al. fabricated PCL based bioresorbable DECS that was implanted into the porcine femoral artery for an in vivo evaluation and characterization.[27] However, the practical feasibilities of PCL bioresorbable DECS have met with limited success because of its poor mechanical strength.

Several key strategies have been proposed throughout the years to improve the tensile strength, radial force, modulus, and energy at break of PCL.[28] Composite based PCL scaffolds such as PCL/gelatin nanofibers infused PCL framework, PCL coated with gelatin and mucic acid, PCL/gelatin/bacterial cellulose/hydroxyapatite, PCL/hydroxyapatite and PCL/gelatin/carboxymethyl chitin/hydroxyapatite exhibited excellent machinal properties, enhanced cellular proliferation and infiltration and were utilized as orthopedic implants.[14,29–32] A variety of polymer/co-polymer blends haven been utilized to improve the mechanical properties and produce a biodegradable coating with unique drug elution properties.[33,34] For instance, Guerra et al. proposed the heterogenous polymer composite based on PCL/PLA cardiovascular scaffold with enhanced mechanical properties.[35] Recently, carbon-based conducting fillers have been utilized to enhance permeability, conductivity, and mechanical proprieties of the PCL scaffolds.[36–38] Although these hybrid composite PCL scaffolds offer superior mechanical strength, they have not been explored for controlled drug delivery applications. Because of scaffolds degradation, drug delivery often started with slower diffusion followed by faster diffusion. As the polymer degradation progress, diffusional channels open via the matrix's pores, allowing solvated drug molecules to leave the scaffold through degradation. Thus, the drug release from the scaffolds can be improved by managing the polymer degradation process. For instance, Misra et al. fabricated 3D printed DECS using graphene doped PCL composite.[39] The proposed PCL/graphene scaffolds exhibits excellent superior mechanical characteristics and drug loading capabilities.

Recently, research on CDECS has emerged because it offers various benefits over conventional DECS, including increased efficiency, higher patient compliance, and less toxicity.[40,41] Numerous natural polymers such as collagen, gelatin, albumin, chitosan etc. were widely employed as CDECS compared to synthetic polymers owing to their excellent biocompatibility and lower toxicity.[42] However, to date, experimental demonstration of CDECS using synthetic polymers such as PCL is still very scarce. To the best of our knowledge, there are only a few reports on PCL composites for CDECS applications. For instance, Liu et al prepared 3D printed hydrogel/PCL core–shell structured scaffolds with infrared triggered drug release capabilities for cancer therapy and wound healing.[43] To overcome the limitation of the current state-of-the-art, herein, we have designed gold nanoparticle-decorated carbon nanofibers as the functional additives that reinforces the mechanical strength of PCL cardiovascular scaffolds and provides X-ray visibility and controlled drug release. The fibrous structure was prepared from a predesigned, sulfur-containing conjugated microporous polymer following thermal carbonization, and then the doped sulfur atoms facilitated the introduction of Au nanoparticles, leading to the formation of functional additives. The successful intercalation of functional additives into the PCL matrix was confirmed by several analytical techniques. The functional additives reinforced PCL hybrid nanocomposite exhibits higher effective Young's modulus, toughness, and mechanical strength compared to the bare PCL. The functional additives reinforced PCL was processed into fabricate bioresorbable patient specific cardiovascular scaffolds using a fused deposition modeling (FDM) 3D printing technique. The cytocompatibility of the proposed cardiovascular scaffold was demonstrated by various in vitro and in vivo experiments. Finally, the real-time practical feasibility of the functional additives reinforced cardiovascular scaffold was demonstrated through X-ray imaging and controlled drug delivery applications as shown in Scheme 1.

2. Materials and methods

2.1. Preparation of functional additives

In a typical fabrication process, firstly, the S-CNF was prepared from sulfur-containing microporous conjugated polymers (S-CMP) as described previously.[44] The detailed synthesis procedure is described in detail in the Supporting information. To incorporate microscopic Au particles into the S-CNF, a solution impregnation technique was employed. The required amount (0.3 g) of prepared S-CNF was dispersed in a solution of gold (III) chloride in ethanol (20 mM, 300 mL) via sonication for 30 s. Then, the resulting mixture was kept constant stirring for 24 h at 25 °C. The resulting product was isolated by filtration, flushed with ethanol, and dried under vacuum for 24 h at 25 °C to afford the desired product in a quantitative yield.

2.2. Preparation of functional additives reinforced PCL

To prepare different weight percentages of functional additives reinforced PCL nanocomposite, 1.0 *g* of PCL was dissolved in 5 *mL* of dichloromethane. To which the desired amounts of functional additives (0–3 wt% with respect to the weight of PCL) were dispersed by sonication for 30 *s* at 25 °*C*. After stirring for 30 min at 25 °*C*, the product was isolated by precipitating in cold diethyl ether and dried under vacuum at 25 °*C* overnight. For radiopacity, 10 wt% Iohexol (with respective to PCL) was additionally incorporated into the PCL solution.

2.3. Fabrication of cardiovascular scaffolds

The cardiovascular scaffold based on bare PCL and functional additives reinforced PCL composite was fabricated using custom designed

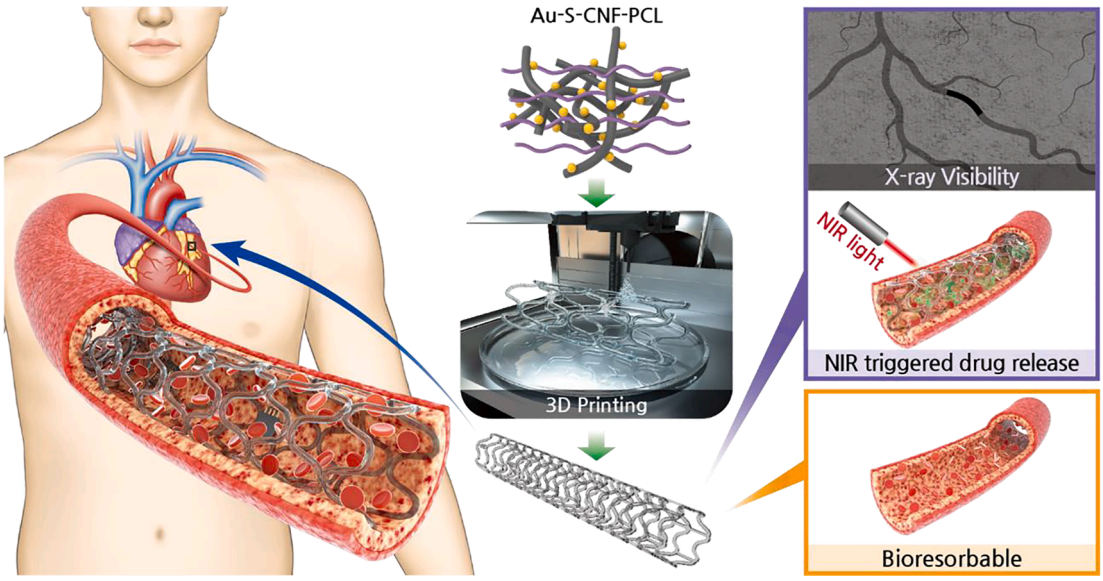

Scheme 1. Our approach utilizes the functional additives reinforced PCL that has been used for the production of patient specific cardiovascular scaffolds fabricated using a emerging field of 3D printing technique for real-time X-ray imaging and targeted therapies such as atherosclerosis, cancer, and tissue engineering.

FDM 3D printing technique at an extrusion pressure of 0.2 *MPa* and temperature of 90 °*C*. The cardiovascular scaffold structure was directly deposited on the print bed using a print head equipped with a dispensing nozzle. The inner diameter of the dispensing nozzle was ~ 300 μ*m*. The cardiovascular scaffold with a thickness of 200 μ*m* and width of 300 μ*m* was directly deposited on a 2.75 *mm* shaft. The dimension of the fabricated scaffold was 3 *mm* in outer diameter and 18 mm, respectively.

2.4. Cell culture

Human umbilical vein endothelial cell (HUVEC, CRL-1730, ATCC, USA) and vascular smooth muscle cell (VSMC, PCS-100–012, ATCC, USA) were utilized for in vitro studies. HUVECs were cultured in BEGM (Bronchial epithelial cell growth medium, CC-3170, Lonza, Swiss) kit containing 1% penicillin/streptomycin antibiotics (P/S, Gibco, NY) at 37 ℃, 5% CO_2, and 95% relative humidity. And VSMCs were cultured in DMEM (10–013-CV, Corning, USA) containing 1% penicillin/streptomycin antibiotics and 10% FBS (Gibco, NY) at 37℃, 5% CO_2, and 95% relative humidity. For CCK-8 assay, HUVEC was seeded at a density of 4 × 103 cells per well and VSMC was seeded at a density of 3.5 × 103 cells per well in a 48-well plate. After 24 *h*, the media was changed and then the cardiovascular scaffold was placed in each well, exposed for 1, 3 and 7 days and cultured. To visualize cell proliferation on the stent surface, 4 × 104 of HUVECs and 4 × 103 of VSMCs were seeded on the cardiovascular scaffold surface, and after 3 *h*, further media was filled. The cells were then attached on the cardiovascular scaffold surface in this way, and were cultured at 37 ℃, 5% CO_2, and 95% relative humidity conditions for 3 days. After the cultured cells were fixed and stained, fluorescence imaging using a confocal microscope was performed.

2.5. Cytotoxicity test

Cytotoxicity test was assessed using cell counting kit-8 assay (CCK8, Dojindo, Japan). After adhering HUVECs and VSMCs into a 48-well plate, a CCK8 assay was performed on each cell group exposed to the PCL cardiovascular scaffold (PCL CVS) with and without NIR irradiation, and 0.5 wt% functional additives reinforced PCL CVS (0.5 wt% FA-PCL CVS) with and without NIR irradiation for 1, 3 and 7 days. Here, NIR light (PSU-W-FC, Changchun new industries CO. ltd., China) was irradiated with 1 W/cm^2 of the power for 30 min. Remove the cardiovascular scaffolds from the each well, and 10% of the media amount of CCK-8 solution was added into each well and then incubated at 37 °*C* for 1 *h*. After incubation, the absorbance of the plate was measured at 450 *nm* using a microplate reader.

2.6. CLSM visualization of cell proliferation on the cardiovascular scaffold films

Cell adhesion and proliferation on cardiovascular scaffolds surface were observed using actin filaments and nucleus staining. The cardiovascular scaffold with HUVECs or VSMCs were rinsed with PBS and then fixed with 4% methanol-free formaldehyde for 30 min. After gently washing the fixed samples with PBS, permeabilized with 0.2% Triton X-100 in PBS for 20 min and rinsed with PBS 3 times. Then the samples were blocked with 1% BSA in PBS for 30 min and rinsed with PBS 3 times. Lastly, cell actin filament and nuclei were stained with rhodamine-phalloidin (Red, R415. Thermofisher), phalloidin 488 (Green, A12379, Thermofisher), and DAPI (Blue) for 1 *h*, respectively. The staining process proceeded at room temperature in the dark. The stained samples were placed on a confocal dish with PBS and observed using a confocal laser scanning microscope (CLSM, LSM 800, Carl Zeiss, Germany). The obtained fluorescence image results were analyzed using Zeiss ZEN black edition software.

2.7. In vitro controlled drug release test

The NIR light (PSU-W-FC, Changchun new industries CO. ltd., China) was used to perform the controlled drug release test. The temperature changes due to the heating effect of the cardiovascular scaffold by NIR light irradiation was observed using a thermal infrared camera (FLIR E60; FLIR system, Inc). The experimental setup used for the in vitro controlled drug release test is shown in Figure S1. For the drug, the doxorubicin hydrochloride (DOX, MedKoo Biosciences, Inc., USA) was used. To coat the DOX onto the cardiovascular scaffold surface, DOX was diluted into the DI-water (10 *mg/mL*). The cardiovascular scaffold was then immersed into the DOX solution at 37 °*C* for 24 *h*. After DOX coating, it was washed 3 times with DI-water for removing the residual DOX. To analyze the coating efficiency of the drug onto the cardiovascular scaffold surface, the drug-coated cardiovascular scaffold was dissolved into the chloroform and then the supernatant was extract. Thereafter, UV–vis absorption spectra (within 350 to 700 *nm* wavelength) was measured by using a microplate reader (Varioskan flash,

Thermo Fisher Scientific Inc., USA). In addition, the amount of DOX coated onto the cardiovascular scaffold surface were determined by measuring the absorbance of the supernatant by UV–vis spectrometry (Lambda 25 UV–vis spectrophotometer, PerkinElmer, Boston, MA)) at 480 *nm* wavelength. Moreover, to analyze the amount of the controlled released drugs by NIR irradiation, DOX coated cardiovascular scaffold was immersed into the PBS solution. After NIR irradiation, 100 μ*L* of supernatant of the DOX released from the cardiovascular scaffolds was collected and their fluorescence was measured by using a microplate reader (Varioskan flash, Thermo Fisher Scientific Inc., USA). The excitation and emission wavelengths of the microplate reader were 490 and 590 *nm*, respectively. Subsequently, 100 μ*L* of PBS solution was refilled. Here, NIR light was irradiated with 3 W/cm^2 of the power for 10 min at 1, 3, 6, and 12 *h*.

2.8. *In vivo controlled drug release test*

All in vivo experiments and animal models were approved by the Chonnam National University Institutional Animal Care and Use Committee (CNU IACUC-YB-2022–26). Blab/c mice (6 weeks old) were purchased from SAMTAKO Co. (SAMTAKO Bio Korea, Osan, Gyeonggi-do, Korea). All animals were housed in cages and rooms with controlled environments. During the in vivo X-ray imaging test, anesthesia of the animals was administered using a tabletop anesthesia system (Harvard Apparatus; Harvard Bioscience Inc., Holliston, MA, USA), which uses N_2O/O_2 mixed with isoflurane. After anesthetization, a 2–3-*cm* incision was made and the cardiovascular scaffold were injected directly in the thoracic cavity. Thereafter, the surgical sites were sutured using the VetbondTM (3 M CO.) tissue adhesive. The real-time X-ray monitoring of the stent in the thoracic cavity of the mouse was performed under X-ray irradiation (C-arm, Ziehm vision RFD, Ziehm Imaging GmbH, Germany).

3. Results and discussion

To improve the mechanical stability and radial force of the cardiovascular scaffold and to enable its use in X-ray imaging and controlled drug eluting applications, reinforced PCL hybrid nanocomposites with varying weight percentages of functional additives were prepared. A three-step protocol method was adapted for the preparation of functional additives reinforced PCL hybrid nanocomposite as shown in Fig. 1**a**. Firstly, the sulfur-doped carbon nanofiber (S-CNF) was prepared from the sulfur-containing conjugated microporous polymer (S-CMP) using a modified version of our published method as described in Supporting Note 1.[44] In general, CMPs comprise rigid π-conjugated skeleton and exhibit high surface area together with unique physical properties. In particular, their chemical structure and global morphology can be controlled via a bottom-up approach adopting using various building blocks or adjusting reaction conditions, which alters macroscopic properties and extends the potential for diverse applications including catalysis, sensing, or storage.[44–49] Here, the elementally engineered CMP (i.e., S-CMP) was further demonstrated as a carbon precursor for the functional additive. In brief, two rigid monomers such as 1,3,5-triethynylbenzene and 2,5-diiodothiophene through the Sonogashira–Hagihara coupling polymerization at 25 °*C* for 24 *h*. The resultant polymer network has a planar like morphology and contains intrinsic sulfur atoms from the thiophene units over the whole structure. The precursor polymer network was subsequently converted

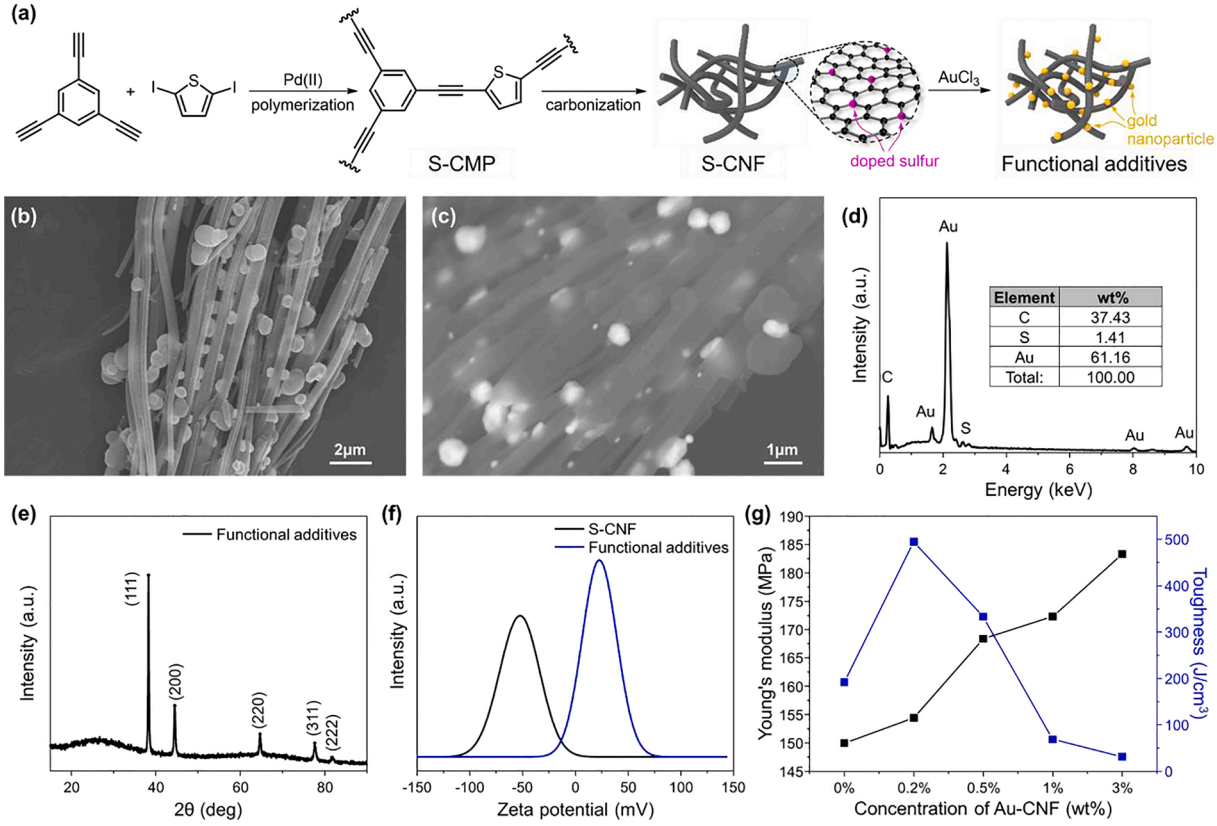

Fig. 1. Preparation, morphological and crystal structure analysis of the functional additives. (a) Detailed fabrication process flow for the preparation of functional additives. (b) Field emission scanning electron micrograph of the prepared functional additives. (c) SEM image of functional additives in backscattered electron mode. (d) Energy dispersive spectra of the prepared functional additives. (e) Powder X-ray diffraction pattern of the functional additives. The miller indices for gold particles shown in the parentheses. (f) Zeta potential data of S-CNF (black) and functional additives (violet). (g) Change in effective Young's modulus (black) and toughness (navy) of the PCL nanocomposites when the concentration of the functional additives varied from 0 to 3.0 wt%. (For interpretation of the references to color in this figure legend, the reader is referred to the web version of this article.)

into S-CNF via heating at 800 °*C* for 3 *h* under nitrogen atmosphere. Then, a solution impregnation technique was employed to prepare the functional additives. Of note, using the intrinsic reducing capability of S atoms doped in CNF and the strong bonding interaction between Au and S, the Au particles can be seeded on the S-CNF without the need for additional exogenous reducing agent.[50,51] Furthermore, the addition of the Au particles would not only reduce latent cytotoxicity but also enhance the dispersibility of S-CNF while suppressing re-aggregation which allowed functional additives to be doped in and reinforce the PCL matrix. Of note, 3D printable polymer composites for bioresorbable stents have been limitedly explored so far and the molecularly designed, carbon-fiber-based hybrid additive have been newly demonstrated in the PCL matrix, as discussed in Table S1.

Overall morphology, crystalline structure, and phase purity of the prepared functional additives were investigated using field emission scanning electron microscope (FESEM), X-ray diffraction (XRD), and X-ray photoelectron spectra (XPS) analysis, respectively. The prepared S-CNF has an anisotropic structure with a diameter in the range of 300–400 *nm* that is adorned with microscopic Au particles as shown in Fig. 1**b**. We further investigated the incorporated Au particles using a backscattered electron (BSE) detector integrated into a FESEM, as shown in Fig. 1**c**. The BSE image's contrast inversion confirms the presence of

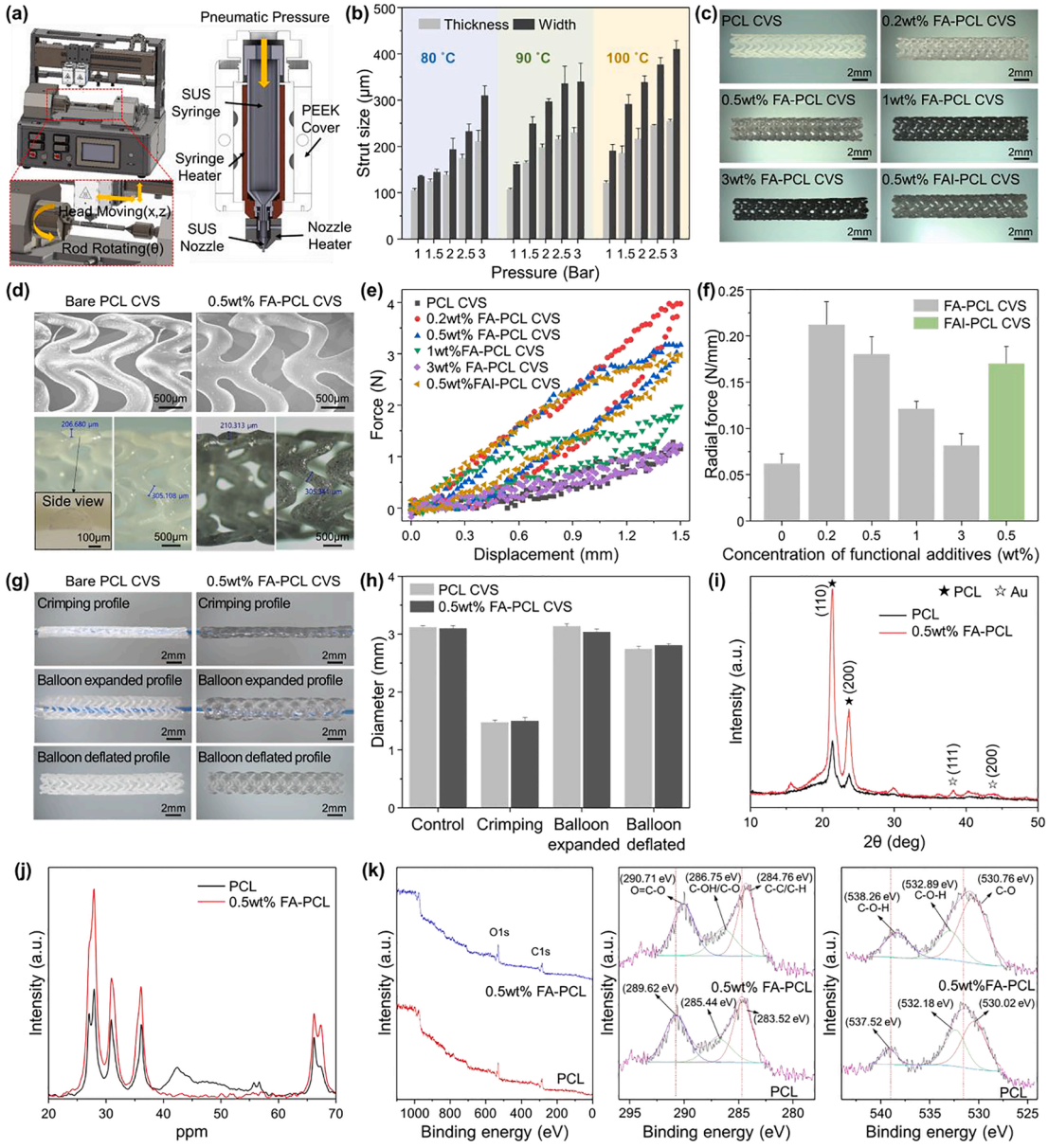

Fig. 2. Mechanical and crystal structure analysis of the bare and functional additives reinforced cardiovascular scaffolds. (a) Prototype model of the custom-made 3D printing machine that has been used for the fabrication of functional additives reinforced PCL scaffold. (b) The bar plot shows the effect of temperature and pressure on cardiovascular scaffolds strut thickness and width at varying functional additives concentration from 0 to 3.0 wt%. (c) The optical images of the PCL cardiovascular scaffolds at varying functional additives concentration from 0 to 3.0 wt%. (d) FESEM images of the bare and 0.5 wt% functional additives reinforced cardiovascular scaffolds, and optical images of the bare and 0.5 wt% functional additives reinforced PCL cardiovascular scaffold strut thickness and width. Inset shows the cross-sectional view of the strut thickness and width. (e, f) Plots shows the radial force of the fabricated cardiovascular scaffolds at varying functional additives concentration from 0 to 3.0 wt%. (g, h) Optical images and bar plots demonstrates the diameter of the fabricated cardiovascular scaffolds based on bare and functional additives reinforced PCL cardiovascular scaffolds at control, crimping, balloon expanded and deflated states. (i-k) Powder X-ray diffraction pattern, ^{13}C solid state NMR, and X-ray photoelectron spectra of the bare PCL and 0.5 wt% functional additives reinforced PCL cardiovascular scaffolds. FA, FAI, CVS in figures represents functional additives, functional additives coated with lohexol and cardiovascular scaffold, respectively.

colloidal Au particles that are ubiquitously embedded on S-CNF. Additionally, when assessed using energy-dispersive X-ray spectroscopy (EDS), the Au nanoparticles were found to be formed and embedded onto the functional additives as shown in Fig. 1**d**, and the atomic ratio of Au/C was determined to be 61.16% from the point analysis of the particle. The strong and sharp diffraction peaks were observed at 38.3, 44.5, 64.7, 77.7, and 81.8° which are in good agreement with the (1 1 1), (2 0 0), (2 2 0), (3 1 1), and (2 2 2) Miller indices of the face-centered cubic (FCC) crystal structure of the embedded Au (Fig. 1**e**).[52] Meanwhile, the functional additives shows the broader diffraction patterns at 24° attributed to the amorphous halo of the carbon matrix.[53] The crystallite size (CS) of the Au particles was calculated using Scherer equation. The obtained CS was found to be ~ 48 *nm*, which not only indicates the formation of microscopic Au particles but would support fine encapsulation of the carbonized fibers with the Au particles. The functional additives were further characterized by the XPS analysis as shown in **Figure S2**. The survey spectra show the photoelectron peaks from S-CNF and functional additives (Fig. S2**a**). In particular, the core-level spectra of S-CNF and functional additives in C1s and O1s regions are deconvoluted into three peaks based on its oxidation states as shown in Fig. S2**b, c**. The peaks at 284.52, 286.25, and 289.36 *eV* can be indexed to -C—C/C═C, -C—S, and -O—C—O/C═O, respectively. The peaks at 530.21, 532.44, 534.62 *eV* can be indexed to O—S, C═O, C-OH/C—O—C, respectively.[54–57] The core-level spectrum of Au 4f electrons, the two peaks at 84.12 and 88.24 *eV* belongs to Au $4f_{7/2}$ and Au $4f_{5/2}$, respectively (Fig. S2**d**).[58,59] The entire Au/C atomic ratio was confirmed as 14.03%, supporting the Au particles embedded onto the carbon skeleton. The incorporation of the Au particles into the S-CNF altered overall surface charge of the S-CNF analyzed by the ζ-potential measurement as shown in Fig. 1**f**. The ζ-potential of the S-CNF was –52.8 *mV* which changed to be + 23.1 *mV* in functional additives after inclusion of the Au particles; further, the size distributions of S-CNF and functional additives are exhibited in **Figure S3**. These findings above support capabilities of the introduction of Au particles into the sulfur-doped fibrous carbon platform and facile preparation of functional additives.[60,61].

The designed functional additives were incorporated into PCL at the concentrations between 0 and 3 wt%. The functional additives were found to dramatically affect mechanical strength of the resulting nanocomposites. For tensile testing, we were able to prepare strip samples using the composites via melt casting in a mold owing to thermoplastic behavior of PCL, (each sample size: 3.6 *mm* × 10 *mm* × 0.6 *mm*) and measure change in mechanical properties as the concentration of functional additives varied as shown in Fig. 1**g**. The pristine PCL strip without functional additives exhibited the effective Young's modulus of 150 *MPa*, which gradually increased then reached 184 *MPa* at 3 wt% of functional additives. The toughness also increased from 192 to 495 $J\ cm^{-3}$ when 0.2 wt% functional additives was added, but significantly decreased after exceeding 0.5 wt% as shown in **Figure S4**. We presume that the additive reinforces the PCL matrix when embedded but potential aggregation of them that could occur above 0.2 wt% disturbs elasticity of the PCL nanocomposites. Overall, the functional additives caused the PCL matrix to be hard yet brittle; the incorporation of 0.5 wt % functional additives notably resulted in the reinforced nanocomposite exhibiting superior mechanical properties (effective Young's modulus, 169 *MPa*; toughness, 334 $J\ cm^{-3}$) to that of other composites. Above the concentration of 0.5 wt%, the composite samples became brittle presumably owing to severe aggregation of the functional additives in the matrix, which hampered intrinsic thermoplastic behavior of PCL matrices. Thus, the toughness values of the samples with greater than 1 wt% functional additives were even lower than that of the pristine PCL sample.

Thermal stability of the fabricated PCL and functional additives reinforced PCL were investigated using thermogravimetry differential thermal (TGA) analysis (**Figure S5**). The TGA profiles revealed that the degradation temperature of the functional additives reinforced PCL were increased compared to the bare PCL. The bare PCL exhibited the degradation temperature at 380 °*C* which is increased to 396 °*C* for 0.2 wt% functional additives was added, but the degradation temperature was gradually decreased further increasing the functional additives weight percentage. The degradation temperature for 0.5, 1.0, and 3.0 wt % functional additives reinforced PCL was 394 °*C*, 387 °*C*, and 384 °*C*, respectively. As discussed earlier, the incorporation of functional additives increased the mechanical strength, impede the degradation process in the PCL matrix, thus increasing the thermal stability of the polymer matrix.[62,63] Additionally, given the functional additive's microporous carbonized framework, we evaluated the internal porosity of a 0.5 wt% functional additives reinforced PCL using nitrogen adsorption–desorption isotherms measured at 77 *K* as shown in **Figure S6**. The pristine PCL was found to be nonporous and to have a minimal interaction with the adsorbate gas, like that of other polymers such as polyethylene, which remained unchanged following addition of 0.5 wt% of functional additives. These findings, however, suggest that the functional additives were distributed uniformly throughout the composite, rather than aggregating and rising to the surface.

The resultant functional additives reinforced PCL was processed into fabricate cardiovascular scaffolds using a FDM 3D printing technique as shown in Fig. 2**a**. Computer aided design software design of the cardiovascular scaffold structure information that has been transferred to the 3D printing machine is shown in **Figure S7.** The bare PCL- and functional additives reinforced PCL-based cardiovascular scaffolds were deposited directly on the print bed using a print head equipped with a dispensing nozzle. The cardiovascular scaffold strut thickness and width were controlled by regulating the movement of the print head in x- and y-direction and print bed rotational speed. Struts with a smaller thickness and width are more affordable. However, a series of animal and clinical investigations indicated that thinner struts resulted in decreased restenosis rates. Therefore, the strut thickness and width have been optimized by controlling polymer melting temperature and pneumatic pressure of the nozzle that extracts the polymer material as shown in Fig. 2**b** and as described in detail in the supporting note 2. Based on the experimental findings, the best degree of completeness with the ideal cardiovascular scaffold width (300 μ*m*) and thickness (200 μ*m*) was reached at a processing temperature of 90 °*C* and a pressure of 0.2 *MPa*. The optical images of the fabricated bare PCL scaffolds and functional additives reinforced PCL scaffolds are shown in Fig. 2**c**. FESEM images reveals the well faceted and uniform shape and size of the cardiovascular scaffold's struts based on bare and 0.5 wt% functional additives reinforced PCL (Fig. 2**d**). The optical images show the strut thickness and width of the bare and 0.5 wt% functional additives reinforced cardiovascular scaffolds. The inset in Fig. 2**d** shows the strut cross-sectional view of the PCL based cardiovascular scaffolds.

To overcome lesion resistance and elastic recoil, a high radial force and complete cardiovascular scaffold apposition are critical requirements for optimal scaffold implantation.[64–66] Radial scaffold strength is largely determined by three factors: the materials used for the scaffold fabrication, strut thickness and scaffold architecture. Therefore, the radial force of the fabricated scaffolds based on functional additives reinforced PCL at the concentrations between 0 and 3 wt% was measured as a function of radial displacement using a radial strength tester (Ez-Test EZ-L, Shimadzu) as shown in Fig. 2**e, f**. During the measurement the outer diameter of the cardiovascular scaffolds was decreased from 3 to 1.4 *mm* at a compression rate of 0.1 *mm/s*. Three cardiovascular scaffolds radial strength readings were averaged to determine the radial strength at each experimental point. The radial force of the bare PCL cardiovascular scaffold was 0.065 *N/m*, which increased to 0.21 *N/m* at 0.2 wt% functional additives incorporation. However, after surpassing 0.2 wt%, the radial force of the PCL scaffold was decreased. Although, 0.5 wt% functional additives reinforced PCL cardiovascular scaffold exhibiting lower radial force compared to that of 0.2 wt% functional additives reinforced PCL cardiovascular scaffold but exhibiting superior mechanical properties (effective Young's modulus

and toughness) to that of other composites as shown in Fig. 2**f**. Therefore, 0.5 wt% functional additives reinforced PCL is considered the optimal composite for cardiovascular scaffold production. The radial force of the 0.5 wt% functional additives reinforced PCL with lohexol reduced compared to the cardiovascular scaffold without lohexol. But still displays appropriate radial force and significantly higher than bare PCL that can sustain diameters of the expanded blood artery. Further, the mechanical stability of the bare PCL and 0.5 wt% functional additives reinforced PCL cardiovascular scaffolds were investigated through crimping and expansion test as shown in Fig. 2**g**, h. The fabricated cardiovascular scaffolds were inserted into a balloon catheter and placed inside a radial compression machine (Model: RJ, Blockwise). All the experiments were carried out at a temperature of 30 $^{\circ}C$ and pressure 15 *psi*. The bare and 0.5 wt% functional additives reinforced PCL cardiovascular scaffolds under crimping, balloon expanded, and balloon deflated profiles are shown in Fig. 2**g**. The diameter of the bare PCL and 0.5 wt% functional additives reinforced PCL cardiovascular scaffolds exhibits similar behavior when the scaffolds were compressed from a diameter of 3 *mm* to 1.5 *mm*. The diameters of bare and 0.5 wt% functional additives reinforced PCL cardiovascular scaffolds were increased to 3.1 *mm* through balloon expansion and recovered to 2.74 and 2.81 *mm* immediately after withdrawing balloon-expanding. The dynamic mechanical analysis of the functional additives reinforced cardiovascular scaffold reveals considerable improvement for mechanical strength enhancements such as superior toughness and radial force across all geometries of PCL due to the randomly intercalated functional additives in the PCL polymeric network. Additionally, the improved yield strength functional additives reinforced cardiovascular scaffold could be attributed to the decreased chain mobility of the polymer, being "locked" in position by the functional additives.

To confirm this hypothesis, we carried out the FESEM, XRD, nuclear magnetic resonance (NMR), and XPS analysis. The morphology of the bare and 0.5 wt% functional additives reinforced PCL cardiovascular scaffold was observed by FESEM. The bare scaffold exhibited a smooth surface as shown in **Figure S8a, b**. The corresponding elemental mapping and EDX spectra are shown in **Figure S8c**-g. The atomic ratio of carbon and oxygen in the bare PCL was determined to be 53.26% and 46.74%, respectively as shown in **Figure S9**. FESEM images of 0.5 wt% functional additives reinforced PCL scaffold shows that the carbon and Au is randomly decorated in the PCL matrix as shown in **Figure S10a, b**. Besides, the FESEM indicates not only successful incorporation of functional additives into the PCL matrix, but also the S-CNF act as a carrier template that effectively control the dispersion of Au particles and thus prevents their aggregation. Elemental mapping of the 0.5 wt% functional additives reinforced PCL scaffold is shown in **Figure S10c**. It indicates the uniform distribution of carbon, oxygen, and gold presence in the hybrid nanocomposite. Elemental maps of the homogeneously distributed individual carbon, oxygen, and gold elements in the functional additives reinforced PCL scaffold is shown in **Figure S10d-f**. EDS spectra of the prepared 0.5 wt% functional additives reinforced is shown in **Figure S10g**. The atomic ratio of carbon, oxygen and Au in the hybrid nanocomposite was determined to be 70.76%, 24.01%, and 5.24%, respectively as shown in **Figure S11**.

To further confirm the successful intercalation of functional additives into PCL matrix, the prepared samples were investigated using XRD analysis as shown in Fig. 2**i**. The bare and functional additives reinforced PCL scaffolds shows the diffraction patterns at 21.9° and 24.2° corresponding to the (1 1 0) and (2 0 0) planes of the orthorhombic crystal structure.[67–68] The samples containing different amount of functional additives shows the same diffraction patterns at 21.9° and 24.2°, suggesting that the crystallization of bare PCL not affected by the incorporation of functional additives. The functional additives reinforced PCL scaffolds reinforced hybrid nanocomposite shows the diffraction patterns at 38.1, 44.5, 64.8 and 77.5° corresponding to the (1 1 1), (2 0 0), (2 2 2) and (3 1 1) planes of FCC Au crystal structure.[69] However, the full width at half maximum (FWHM) of the (1 1 0) and (2 0 0) planes increased with increasing the wt% of functional additives (up to 1 wt%) in the PCL composite indicating that the successful intercalation of functional additives into the PCL matrix and subsequent detangling of the polymer chains because of incorporation of functional additives (**Figure S12**).

The effect of incorporation of functional additives into the PCL matrix further investigated using ^{13}C solid-state NMR Spectra analysis. The NMR spectra of the PCL and different concentration of functional additives ranging from 0 to 3 wt% reinforced PCL in direct-polarization magic-angle spinning (DPMAS) and cross-polarization magic-angle spinning (CPMAS) mode are shown in Fig. 2**j** and **Figure S13**. The DPMAS and CPMAS spectra provides the information about nature of carbon atoms present and dipole–dipole interaction in the samples, respectively.[39] The ^{13}C NMR spectra in both DPMAS and CPMAS mode shows the well-defined peaks at 27.67, 30.73, 35.88, 42.31, 56.68, 66.21, 129.95, and 148.65, *ppm*, which are consistent with the previous reports.[70–72] The FWHM of the PCL peaks becomes much broader with increasing concentrations of functional additives, indicating the existence of a significant amount of disordered local environments in close proximity to carbon sites. Besides, the peaks in the ranges of 38–60 and 150 *ppm* disappeared in both CPMAS and DPAMS mode with the incorporation of functional additives, demonstrating that the crystal structure of PCL is affected by the inter - planar addition of functional additives to PCL matrix.

The strong chemical and electronic interaction between the functional additives and the PCL were further confirmed by the XPS analysis. The survey spectra show the photoelectron peaks from caron and oxygen which are arise from the backbone of PCL$(C_6H_{10}O_2)_n$ structure. The photoelectron peaks corresponding to the sulfur and Au were missing could be due to the less amount functional additives present in the PCL matrix which is beyond the detection limit of XPS instrument (Fig. 2**k**). The C1s core level spectra are deconvoluted into three peaks depending on their functional states. The O1s core-level spectra of bare PCL and 0.5 wt% functional additives reinforced PCL cardiovascular scaffold was deconvoluted into three peaks depending on their oxidation states. The photoelectron peaks at 530.76, 532.18, 537.53 eV can be indexed to the C—O, C═O, and C—O—H, respectively.[73] The peak observed in bare PCL polymer at ~ 289.62, 285.44, 283.52 eV can be indexed to the O═C-O, C-OH/C—O, and C—C/C—H, respectively.[74,75] These photoelectron peaks in 0.5 wt% functional additives reinforced PCL is shifted to higher binding energy ~ 1. 1 eV indicating the strong chemical and electronic interaction between the functional additives and PCL could be attributed to the interlayer intercalation of functional additives in the PCL matrix. The interlayer incorporation of functional additives in PCL matrix would be advantageous for sustained and controlled drug release when layer by-layer degradation of PCL layer after being implanted in a blood artery.

The elastic recovery rate of the proposed cardiovascular scaffolds based on PCL and 0.5% functional additives-reinforced PCL was measured using a customized radial compression device (Ez-Test EZ-L, Shimadzu). Measurements were conducted under the following experimental conditions: Length of scaffold is 18 mm, diameter of scaffold is 3 mm, velocity of displacement is 1 mm min^{-1}, and compression distance is 1.5 mm. The presser foot was designed to compress cardiovascular scaffolds to 1.5 mm and hold for 30 s, then retract to the original position at 1 mm min^{-1}, and the diameter (D) of the scaffold was measured. The following equation was used to obtain the elastic recovery rate (R) of the cardiovascular scaffolds.

$$R = \frac{d}{D} \times 100\%$$

where R is the elastic recovery rate, D and d represents the diameter of the cardiovascular scaffold before and after compression. Figure S14 illustrates the elastic recovery of the proposed cardiovascular scaffolds based on PCL and 0.5 wt% functional additives reinforced PCL

nanocomposites during cyclic compression testing. Following the first compression, the elasticity of both cardiovascular scaffolds dropped to 95% and remained at that level during successive compression cycles.

The mechanical characteristics of the fabricated PCL and functional additives reinforced PCL hybrid nanocomposite under biodegradable condition was examined by measuring the radial force of the cardiovascular scaffolds over time. The cardiovascular scaffolds were immersed in a PBS solution for 10 days, and the radial force was evaluated at regular intervals, as shown in Figure S15. The biodegradability rate of the fabricated cardiovascular scaffolds was looks similar in both bare PCL and functional additives reinforced PCL composite. The biodegradability test demonstrates that (i) PCL-based scaffolds could not disastrously degrade under physiological conditions and (ii) the addition of the carbon nanofibers could retard the degradation, both of which provide enough time for the scaffold after being inserted in the target lesion. The surface wettability and energy of the cardiovascular scaffolds are of prime importance when biocompatibility of the material is determined. The water contact angle (WCA) and surface energy of the bare PCL and 0.5 wt% functional additives reinforced PCL cardiovascular scaffolds are shown in Figure S15. The WCA of the bare PCL cardiovascular scaffold was 82.06 ± 0.75, whereas the functional additives reinforced PCL cardiovascular scaffolds was 71.14 ± 1.9. Besides, the functional additives reinforced PCL cardiovascular scaffold exhibits higher surface energy compared to bare PCL cardiovascular scaffolds demonstrating that the incorporation of functional additives into the PCL matrix reduced the contact angle and rendering the PCL membrane hydrophilic and suitable for cell culture.

The cytocompatibility of the fabricated cardiovascular scaffolds based on PCL CVS and 0.5 wt% FA-PCL CVS was confirmed through cytotoxicity test. The cell growth, proliferation, and viability of HUVEC and VSMC were analyzed using CCK8 assay and confocal laser scanning microscopy (CLASM) visualization on day 1, 3, and 7. The cell viability of HUVEC and VSMC on the PCL CVS and 0.5 wt% FA-PCL CVS, with and without NIR irradiation, was between 70% and 90% compared to the cell viability of the control group (only cultured cells) demonstrates that the fabricated cardiovascular scaffolds exhibit biocompatibility and no cytotoxicity as shown in Fig. 3(a, b). Although compared to the control group both PCL and 0.5 wt% functional additives reinforced PCL cardiovascular scaffolds surfaces showed reduced viability, a consistent increase in cell proliferation on both surfaces was depicted. In addition, a slightly higher proliferation rate was observed in functional additives incorporated PCL cardiovascular scaffold signifying that the functional additives reduced the inherent hydrophobicity of the bare PCL and provides better cell–cell interaction owing to its conductive nature. Based on these findings, proliferation of HUVEC and VSMC on the cardiovascular scaffold surface after 3 days of culture was also visualized using CLSM imaging, as shown in Fig. 3c. Both HUVECs and VSMCs adhered and proliferated effectively on the surfaces of PCL and functional additives reinforced PCL cardiovascular scaffolds. The in vitro experiments have demonstrated that the fabricated scaffolds are biocompatible since they are not cytotoxic to intravascular cells. This not only demonstrates the feasibility of proposed cardiovascular scaffolds use in animal models, but also implies that the material is stable enough for its use in medical applications. Fig. 3d shows optical images of the 0.5 wt% functional additives reinforced PCL cardiovascular scaffolds with varying iohexol concentration ranging from 5 to 20%. It is now well established that the cardiovascular scaffolds with higher concentration of iohexol can be easily visualized in X-ray imaging. However, adding more amount of iohexol could affect the printability of the polymer material. The cardiovascular scaffold loaded with 10% of iohexol is widely used as an optimized contrast medium for X-ray imaging. The proposed 0.5 wt% functional additives reinforced PCL cardiovascular scaffold with 10% iohexol was immersed in PBS solution and implanted into the thoracic cavity of the mouse, respectively, and then examined using the c-arm imaging equipment to verify its visibility under real-time X-ray for in vitro and in vivo environments, as shown in Fig. 3e, f. The detailed experimental procedure for the X-ray imaging is described in the materials and method section. Real-time X-ray imaging of the 0.5 wt% functional additives reinforced PCL cardiovascular scaffold indicated that an X-ray contrast agent (Iohexol, 10%)-loaded scaffold can be monitored with real-time X-ray imaging.

Finally, the 0.5 wt% functional additives reinforced PCL cardiovascular scaffold was used for the demonstration of NIR-light-triggered controlled drug delivery application as shown in Fig. 4. The bare PCL and functional additives reinforced PCL cardiovascular scaffold was immersed in a 35 *mm* diameter petri-dish filled with PBS. Then, the 0.5 wt% functional additives reinforced PCL cardiovascular scaffolds were irradiated with 808 nm wavelength NIR light (1 W/cm^2) for 200 *s*. The functional additives reinforced PCL cardiovascular scaffold temperature increased owing to the heating effect of NIR light irradiation as shown in Fig. 4**a**. Because of the incorporation of functional additives, the PCL scaffold becomes sensitive to NIR light exposure. The effect of functional additives on the generation of heat was examined by varying the functional additives concentration from 0, 0.2, 0.5, and 1 wt% while maintaining the same NIR light source, intensity, and exposure time. The temperature on the PCL cardiovascular scaffolds with 0, 0.2, 0.5, and 1 wt% functional additives was reached more than 2 °C, 5 °C, 8 °C, and 10 °C within 200 s, respectively as shown in Fig. 4**b, c**.

Secondly, the generation of temperature on the functional additives incorporated PCL scaffold was measured by fixing the amount of functional additive concentration to 0.5 wt% and increasing the power of the NIR light source from 1 to 3 W/cm^2 as shown in Fig. 4**d, e**. The results demonstrate that the 0.5 wt% functional additives reinforced PCL scaffold could effectively and rapidly convert the NIR light into thermal energy, which is necessary to triggered doxorubicin hydrochloride (DOX) drug release from the proposed cardiovascular scaffold using an external NIR light source. The DOX coating on cardiovascular scaffold was optically demonstrated owing its π electron absorption peak (λ ≈480 nm) in the DOX-coated cardiovascular scaffold, but it was not observed in the bare PCL cardiovascular scaffold as shown in Fig. 4**f**. The inset in Fig. 4**f** shows the DOX-coated cardiovascular scaffold and bare scaffold. The surface color of the 0.5 wt% functional additives reinforced PCL cardiovascular scaffold was turned to be red after DOX coating. The DOX coating efficiency onto the 0.5 wt% functional additives reinforced PCL cardiovascular scaffold surface was ~0.012 $\mu g/mm^2$.

Finally, NIR-triggered controlled drug release from the 0.5 wt% functional additives reinforced PCL cardiovascular scaffold was demonstrated as shown in Fig. 4**g**. First, to investigate the premature release of DOX, a time-dependent natural DOX release from the PCL cardiovascular scaffold was measured prior to triggering the NIR light. A spontaneous release of DOX molecules was spotted, without NIR light irradiation, owing to the relatively weak bonding between DOX and the 0.5 wt% functional additives reinforced PCL cardiovascular scaffold. The time dependent study shows that within 60 min, ~22% (3.6% per min) of DOX was released from the cardiovascular scaffold. After that, the release rate was decreased with a total release amount of 30% within 48 *h* (0.28% per min). In contrast, burst release (average 10%) was observed after NIR light irradiation (for 10 min with 3 W/cm^2 power) at 60, 180, 360, and 720 min. Especially, 20% bursting (2% per min) was observed after NIR irradiation at 60 min. In addition, the release rate was also accelerated after NIR irradiation with a total release amount of 60% within 48 *h* and it is 2-folds higher than the natural release. Thus, because of NIR light irradiation, DOX was released owing to the local heating of the PCL cardiovascular scaffolds incorporated with the functional additives, which increased thermal vibration of the polymer chains and thus weakened the binding with drug molecules.

The in vivo controlled drug release was performed using a mouse. The DOX coated 0.5 wt% functional additives reinforced cardiovascular scaffold was implanted into an abdomen of the mouse. The thermal infrared images of the DOX coated 0.5 wt% functional additives reinforced cardiovascular scaffold implanted mouse with and without NIR irradiation (NIR: 808 *nm* wavelength and power of 3 W/cm^2) is shown in

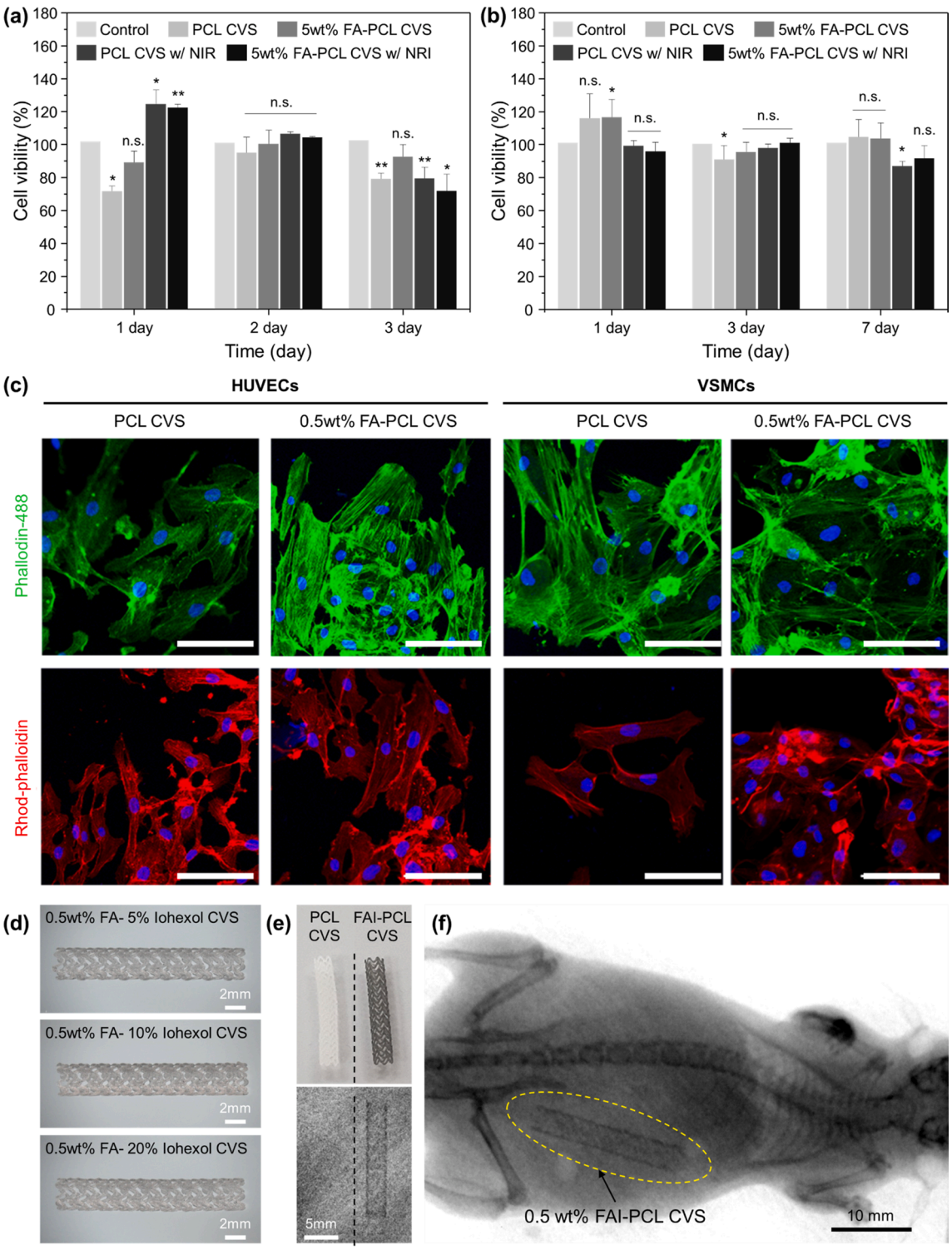

Fig. 3. Cytotoxicity analysis of the fabricated bare and functional additives reinforced cardiovascular scaffolds. Relative cell viability of human umbilical vein endothelial cells (HUVECs) (a) and Vascular smooth muscle cells (VSMCs) (b) after 1, 3, 7 day incubation with the bare and 0.5 wt% functional additives reinforced PCL cardiovascular scaffold with and without NIR irradiation, respectively. n = *4* (for each cell type). The viability of the control (only cells) was set to 100%. $^{*}P < 0.05$ and $^{**}P = 0.0002$. (c) Confocal laser scanning microscopy (CLSM) visualization of HUVECs and VSMCs proliferation on bare and proposed functional additives reinforced PCL cardiovascular scaffold. Actin filaments are seen in red and green (phalloidin-staining), cell nuclei in blue (DAPI-staining). In vitro cell proliferation test of HUVECs and VSMCs grown on functional additives reinforced PCL cardiovascular scaffolds after 3 days of culture. Scale bar = 100 *μm*. (d) Optical images of the 0.5 wt% functional additives reinforced PCL cardiovascular scaffolds with varying iohexol concentration ranging from 5 to 20%. Visibility of the proposed 0.5 wt % functional additives reinforced PCL cardiovascular scaffold with 10% of iohexol under real-time X-ray for in vitro (e) and in vivo (f) environments. w/NIR, FA and CVS in figures represents with near infrared light, functional additives and cardiovascular scaffold, respectively. (For interpretation of the references to color in this figure legend, the reader is referred to the web version of this article.)

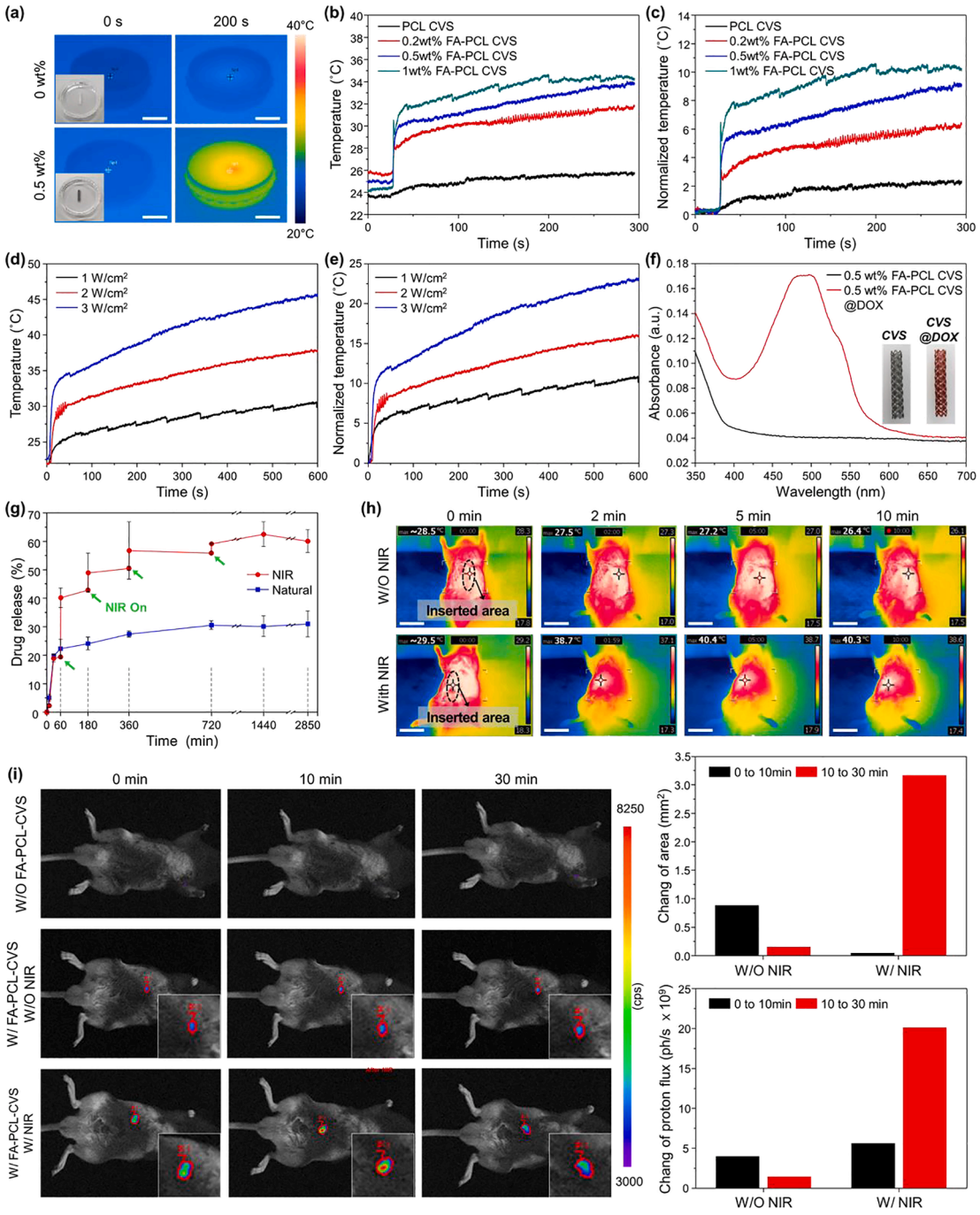

Fig. 4. In vitro and in vivo analysis of the bare and functional additives reinforced cardiovascular scaffolds. (a) Thermal infrared images of the bare scaffolds and 0.5 wt% functional additives reinforced PCL cardiovascular scaffolds (NIR: 808 *nm* wavelength and power of 1 W/cm^2 for 200 *s*). Scale bars: 10 mm. (b, c) Plots of the temperature elevation in the vicinity of the cardiovascular scaffolds by varying the functional additives concentration with 0, 0.2, 0.5, and 1 wt% (NIR: 808 *nm* wavelength and power of 1 W/cm^2). (d, e) Plots of the temperature elevation in the vicinity of the 0.5 wt% functional additives reinforced PCL cardiovascular scaffold by varying the power of the NIR light with 1, 2, and 3 W/cm^2. (f) Light absorption spectrum of the 0.5 wt% functional additives reinforced PCL cardiovascular scaffold with and without the DOX coating. Inset shows the optical images of the 0.5 wt% functional additives reinforced PCL cardiovascular scaffold before and after DOX coating. (g) NIR-triggered drug release from the 0.5 wt% functional additives reinforced PCL cardiovascular scaffold under repeated periodic (red arrows; 60, 180, 360, and 720 min) NIR light irradiation (808 *nm* and 3 W/cm^2). (h) Thermal infrared images of the 0.5 wt% functional additives reinforced PCL cardiovascular scaffold inserted mouse with and without the NIR irradiation for 10 min (NIR: 808 *nm* wavelength and the power of 3 W/cm^2). Scale bars: 20 mm. (i) Fluorescent images of the proposed cardiovascular scaffold at 0, 10, and 30 min time points after the administration of DOX-coated functional additives reinforced scaffold and NIR irradiation (NIR: 808 *nm* wavelength and power of 3 W/cm^2 for 10 min) and their quantitative plots of change of area and photon flux. FA and CVS in figures represents functional additives and cardiovascular scaffold, respectively. (For interpretation of the references to color in this figure legend, the reader is referred to the web version of this article.)

Fig. 4**h**. No temperature difference was found on the mouse without NIR, whereas the temperature was rose to 40 °*C* in the mouse with NIR light exposure for 10 min as shown in movie S1. The signal from the DOX coated 0.5 wt% functional additives reinforced PCL cardiovascular scaffold implanted mouse was detected using an in vivo imaging system for 0, 10, and 30 min as shown in Fig. 4**i**. The mouse was taken out from the in vivo imaging system and captured a thermal image without any NIR light exposure and consider it an initial state (0 min). Then, the in vivo thermal image was captured immediately after exposing the mouse for 10 min. The mouse allowed to stabilize for 20 min in the imaging system to provide sufficient time for diffusing DOX from the functional additives reinforced PCL cardiovascular scaffold. No signal was observed in the mouse without scaffold whereas the DOX fluorescence signal was detected in the DOX coated functional additives reinforced PCL cardiovascular scaffold implanted mouse. The DOX fluorescence signal was increased immediately after NIR light irradiation for 10 min compared to without NIR exposure. It is found that the DOX molecules released from the functional additives reinforced PCL cardiovascular scaffold was aggregated locally, resulting in an increase in fluorescence intensity. Besides, the change in the fluorescent signal from the DOX coated functional additives reinforced PCL cardiovascular scaffold implanted mouse after 20 min of NIR light exposure was substantially higher than from the mouse without NIR light exposure because the released DOX molecules dispersed throughout the organ. The in vitro and in vivo analysis confirmed that the functional additives reinforced PCL cardiovascular scaffold can be effectively used for controlled drug delivery applications such as atherosclerosis, cancer, and tissue engineering.

4. Conclusion

The functional additives reinforced PCL hybrid nanocomposites were prepared by a facile preparation method. The successful intercalation of functional additives into the PCL matrix was confirmed by various analytical techniques. The 0.5 wt% functional additives reinforced PCL nanocomposite exhibited excellent mechanical strength compared to that of other composites. The patient customized functional additives reinforced PCL cardiovascular scaffold was fabricated using a FDM 3D printing technique. The surface of functional additives reinforced PCL based cardiovascular scaffold was chemically stable, cytocompatibility, and favoured adhesion, proliferation, and differentiation of cells. The in vitro and in vivo experiments proved the viability of the proposed functional additives reinforced PCL cardiovascular scaffolds for usage in animal models and in a variety of medicinal applications. Due to its X-ray visibility, the implanted functional additives reinforced PCL cardiovascular scaffold in the mouse thoracic cavity was monitored in real time. The controlled drug delivery from the proposed cardiovascular scaffolds was realized by NIR light irradiation. The proposed cardiovascular scaffolds provide the platform for localized therapy such as atherosclerosis, cancer, and tissue engineering.

Declaration of competing interest

The authors declare that they have no known competing financial interests or personal relationships that could have appeared to influence the work reported in this paper.

Declaration of Competing Interest

The authors declare that they have no known competing financial interests or personal relationships that could have appeared to influence the work reported in this paper.

Data availability

Data will be made available on request.

Acknowledgements

This study was supported through a National Research Foundation of Korea (NRF) grant funded by the Korean government (MSIT) (No. 2020R1A5A8018367).

Appendix A. Supplementary data

Supplementary data to this article can be found online at https://doi.org/10.1016/j.cej.2022.140118.

References

[1] I. Akoumianakis, M. Polkinghorne, C. Antoniades, Nat. Rev. Cardiol. (2022), https://doi.org/10.1038/s41569-022-00718-5.
[2] S.M. Manemann, Y. Gerber, S.J. Bielinski, A.M. Chamberlain, K.L. Margolis, S. A. Weston, J.M. Killian, V.L. Roger, BMC Public Health 21 (2021) 1031.
[3] G. Santulli, J. Cardiovasc. Dis. 1 (2013) 1.
[4] G.K. Hansson, Cardiovasc. Res. 117 (2021) e166.
[5] P. Libby, Cardiovasc. Res. 117 (2021) 2525.
[6] X. Chen, B. Assadsangabi, Y. Hsiang, K. Takahata, Adv. Sci. 5 (2018) 1700560.
[7] M.-K. Hong, G.S. Mintz, C.W. Lee, D.-W. Park, K.-M. Park, B.-K. Lee, Y.-H. Kim, J.-M. Song, K.-H. Han, D.-H. Kang, S.-S. Cheong, J.-K. Song, J.-J. Kim, S.-W. Park, S.-J. Park, Circulation. 113 (2006) 414.
[8] S. Windecker, P.W. Serruys, S. Wandel, P. Buszman, S. Trznadel, A. Linke, K. Lenk, T. Ischinger, V. Klauss, F. Eberli, R. Cotri, W. Wijns, M.-C. Morice, C.D. Mario, S. Davies, R.-J.V. Geuns, P. Eerdmans, G.-A. van Es, B. Meier, P. Jüni, Lancet 372 (2008) 1163.
[9] A. Rodriguez-Granillo, B. Rubilar, G. Rodriguez-Granillo, A.E. Rodriguez, World J. Cardiol. 3 (2011) 84.
[10] T. Muramatsu, Y. Onuma, Y.J. Zhang, C.V. Bourantas, A. Kharlamov, R. Diletti, V. Farooq, B.D. Gogas, S. Garg, H.M. Garcia-Garcia, Y. Ozaki, P.W. Serruys, Rev. Esp Cardiol. 66 (Engl Ed) (2013) 483.
[11] P. Roopmani, S. Satheesh, D.C. Raj, U.M. Krishnan, ACS Biomater. Sci. Eng. 5 (2019) 2899.
[12] H. Huang, G. Li, Q. Ji, D. Bian, S. Guan, O. Kulyasova, R.Z. Valiev, J. V. Rau, Y. Zheng, Acta Biomater, https://doi.org/10.1016/j.actbio.2022.08.041.
[13] J. Zong, Q. He, Y. Liu, M. Qiu, J. Wu, B. Hu, Mater. Today Bio. 16 (2022), 100368.
[14] D. Gupta, J. Bellare, Bioprinting 24 (2021) e00175.
[15] E. Díaz, I. Sandonis, M.B. Valle, J. Nanomater. 2014 (2014) 185.
[16] A. Ostafinska, I. Fortelny, M. Nevoralova, J. Hodan, J. Kredatusova, M. Slouf, RSC Adv. 5 (2015) 98971.
[17] C. Pitt, A. Schindler, Capronor: a biodegradable delivery system for levonorgestrel, in: Long Act. Contracept. Deliv. Syst., Harper and Rao Philadelphia, PA, 1984, p. 63.
[18] B.S. Jang, J.E. Jeong, S. Ji, D. Im, M.K. Lee, S.A. Park, W.H. Park, Mater. Des. 195 (2020), 109005.
[19] [M. S. Saveleva, A. N. Ivanov, J. A. Chibrikova, A. A. Abalymov, M. A. Surmeneva, R. A. Surmenev, B. V. Parakhonskiy, M. V. Lomova, A. G. Skirtach, I. A. Norkin, Macromol. Biosci 21 2021 2100266.
[20] C.M. Brougham, T.J. Levingstone, N. Shen, G.M. Cooney, S. Jockenhoevel, T. C. Flanagan, F.J. O'Brien, Adv. Healthc. Mater. 6 (2017) 1700598].
[21] A.J. Guerra, J. Farjas, J. Ciurana, Opt. Laser Technol. 95 (2017) 113.
[22] A.J. Guerra, J. Ciurana, Mater. Des. 137 (2018) 430.
[23] A.W. Martinez, E.L. Chaikof, Wiley Interdiscip. 3 (2011) 256.
[24] C. Wang, L. Zhang, Y. Fang, W. Sun, Engineering 7 (2021) 979.
[25] R.V. Lith, E. Baker, H. Ware, J. Yang, A.C. Farsheed, C. Sun, G. Ameer, Adv. Mater. Technol. 1 (2016) 1600138.
[26] C. Pan, Y. Han, J. Lu, Micromachines 12 (2021) 770.
[27] S.A. Park, S.J. Lee, K.S. Lim, I.H. Bae, J.H. Lee, W.D. Kim, M.H. Jeong, J.-K. Park, Mater. Lett. 141 (2015) 355.
[28] C. Wan, B. Chen, Biomed. Mater. 6 (2011), 055010.
[29] Y. Yu, S. Hua, M. Yang, Z. Fu, S. Teng, K. Niu, Q. Zhao, C. Yi, RSC Adv. 6 (2016), 110557.
[30] B. Ashwin, B. Abinaya, T.P. Prasith, S.V. Chandran, L.R. Yadav, M. Vairamani, S. Patil, N. Selvamurugan, Int. J. Biol. Macromol. 162 (2020) 523.
[31] Z. Jiao, B. Luo, S. Xiang, H. Ma, Y. Yu, W. Yang, Adv. Ind. Eng. Poly. Res. 2 (2019) 196.
[32] A.M. Cakmak, S. Unal, A. Sahin, F.N. Oktar, M. Sengor, N. Ekren, O. Gunduz, D. M. Kalaskar, Polymers 2020 (1962) 12.
[33] A. Akinapelli, J.P. Chen, K. Roy, J. Donnelly, K. Dawkins, B. Huibregtse, D. Hou, Curr Cardiol Rev 13 (2017) 139.
[34] H.W. Toh, D.W.Y. Toong, J.C.K. Ng, V. Ow, S. Lu, L.P. Tan, P.E.H. Wong, S. Venkatraman, Y. Huang, H.Y. Ang, Euro. Poly. J. 146 (2021), 110249.
[35] A.J. Guerra, P. Cano, M. Rabionet, T. Puig, J. Ciurana, Materials 11 (2018) 1679.
[36] L. Hua, W. Kai, Y. Inoue, J. Appl. Polym. Sci. 2007 (1880) 106.
[37] W.H. Kai, Y. Hirota, L. Hua, Y. Inoue, J. Appl. Polym. Sci. 107 (2008) 1395.
[38] S. Sayyar, E. Murray, B.C. Thompson, S. Gambhir, D.L. Officer, G.G. Wallace, Carbon 52 (2013) 296.
[39] S.K. Misra, F. Ostadhossein, R. Babu, J. Kus, D. Tankasala, A. Sutriso, K.A. Walsh, C.R. Bromfield, D. Pan, Adv. Healthcare Mater. 6 (2017) 1700008.

[40] X.L. Feng, F.T. Lv, L.B. Liu, H.W. Tang, C.F. Xing, Q.O. Yang, S. Wang, ACS Appl. Mater. Interfaces 2 (2010) 2429.
[41] X.D. Xu, L.A. Liang, C.S. Chen, B. Lu, N.L. Wang, F.G. Jiang, X.Z. Zhang, R.X. Zhuo, ACS Appl. Mater. Interfaces 2 (2010) 2663.
[42] A.K. Mahanta, S. Senapati, P. Paliwal, S. Krishnamurthy, S. Hemalatha, P. Maiti, Mol. Pharm. 16 (2019) 327.
[43] C. Liu, Z. Wang, X. Wei, B. Chen, Y. Luo, Acta Biomater. 131 (2021) 314.
[44] H.J. Kim, G.B. Choi, J.-H. Wee, S. Hong, J. Park, Y.A. Kim, H. Kim, ChemSusChem 14 (2021) 624.
[45] J.-S.-M. Lee, A.I. Cooper, Chem. Rev. 120 (4) (2020) 2171–2214.
[46] S. Jeong, J.A. Chae, H.J. Kim, D. Jung, Y.A. Kim, E. Choi, H. Kim, Anal. Chem. 93 (2021) 13513–13519.
[47] J.A. Chae, S. Jeong, H.J. Kim, T. Tojo, Y. Oh, W.S. Chi, H. Yoon, H. Kim, Polym. Chem. 12 (2021) 2464–2470.
[48] J.A. Chae, Y. Oh, H.J. Kim, G.B. Choi, K.M. Lee, D. Jung, Y.A. Kim, H. Kim, Polym. Chem. 10 (2019) 5142–5150.
[49] K.M. Lee, H.J. Kim, C.-S. Kang, T. Tojo, J.A. Chae, Y. Oh, M.C. Cha, K.S. Seung, Y. A. Kim, H. Kim, Polym. Chem. 10 (2019) 852–859.
[50] X. Liu, L. Dai, Nat. Rev. Mater 1 (2016) 16064.
[51] J.R. Reimers, M.J. Ford, A. Halder, J. Ulstrup, N.S. Hush, PNAS 113 (2016) E1424.
[52] M. Hakamada, M. Mabuchi, Nano Letters 6 (2006) 882.
[53] A. Shanmugasundaram, D.-S. Kim, N.D. Chinh, J. Park, Y.-J. Jeong, J.J. Piao, D. Kim, D.W. Lee, Chem. Eng. J. 421 (2021), 127740.
[54] L. Tao, Y. Yang, H. Wang, Y. Zheng, H. Hao, W. Song, J. Shi, M. Huang, D. Millin, Energy Storage Mater. 27 (2020) 212.
[55] A. Shanmugasundaram, P. Basak, S.V. Manorama, B. Krishna, S. Sanyadanam, ACS Appl. Mater. Interfaces 7 (2015) 7679.
[56] A. Shanmugasundaram, S.V. Manorama, D.-S. Kim, Y.-J. Jeong, D.-W. Lee, Chem. Eng. J. 448 (2022), 137736.
[57] A. Shanmugasundaram, N.D. Chinh, Y.-J. Jeong, T.F. Hou, D.-S. Kim, D. Kim, Y.-B. Kim, D.-W. Lee, J. Mater. Chem. A 7 (2019) 9263.
[58] O.F. Odio, L. Lartundo-Rojas, P. Santiago-Jacinto, R.E. Martínez, J. Phys. Chem. C 118 (2014) 2776.
[59] S. Arunkumar, T.F. Hou, Y.-B. Kim, B. Choi, S.H. Park, S. Jung, D.-W. Lee, Sens. Actuators B 243 (2017) 990.
[60] Y. Hu, J. Yang, J. Tian, L. Jia, J.-S. Yu, Carbon 77 (2014) 775.
[61] N.T.N. Anh, R.-A. Doong, ACS Appl. Nano Mater. 1 (2018) 2153.
[62] J.Y. Liu, L. Reni, Q. Wei, J.L. Wu, S. Liu, Y.J. Wang, G.Y. Li, Express Polym Lett 5 (2011) 742.
[63] H. Peng, Y. Han, T. Liu, W.C. Tjiu, C. He, Ther- mochim Acta 502 (2010) 1.
[64] R. Rieu, P. Barragan, C. Masson, J. Fuseri, V. Garity, M. Silvestri, P. Roquebert, Catheter. Cardiovasc. Interv. 46 (1999) 380.
[65] G. Kalmár, F. Hübner, W. Voelker, J. Hutzenlaub, J. Teubner, T. Poerner, T. Süselbeck, M. Borggrefe, K.K. Haase, J. Vasc. Interv. Radiol. 13 (2002) 499.
[66] T. Watson, M.W.I. Webster, J.A. Ormiston, P.N. Ruygrok, J. T. Open Heart 4 (2017) e000680.
[67] X. Li, W. Liu, Y. Li, W. Lan, D. Zhao, H. Wu, Y. Feng, X. He, Z. Li, J. Li, F. Luo, H. Tan, J. Mater. Chem. B 8 (2020) 5117.
[68] Y.-F. Li, M. Rubert, H. Aslan, Y. Liu, K.A. Howard, M. Dong, F. Besenbacher, M. Chen, Nanoscale 6 (2014) 3392.
[69] P. Manjula, S. Arunkumar, S.V. Manorama, Sens. Actuators B 152 (2011) 168.
[70] C. De Kesel, C. Lefevre, J. Nagy, C. David, Polymer 1999 (1969) 40.
[71] C.-S. Wu, Polymer 46 (2005) 147.
[72] S. Sinnwell, A.J. Inglis, T.P. Davis, M.H. Stenzel, C. Barner-Kowollik, Chem. Commun. (2008) 2052–2054.
[73] L. Bech, T. Meylheuc, B. Lepoittevin, P. Roger, J. Polym Sci Pol Chem 45 (2007) 2172.
[74] B.Q.H. Nguyen, A. Shanmugasundaram, T.-F. Hou, J. Park, D.-W. Lee, Chem. Eng. J. 373 (2019) 68.
[75] S. Bhatt, J. Pulpytel, M. Mirshahi, F. Arefi-Khonsari, ACS Macro Lett. 1 (2012) 764.